AFRL-RZ-WP-TP-2010-2146

PROGRESS IN APPLYING TUNABLE DIODE LASER ABSORPTION SPECTROSCOPY TO SCRAMJET ISOLATORS AND COMBUSTORS

Michael S. Brown, Skip Williams, Chadwick D. Lindstrom, and Dominic L. Barone

Propulsion Sciences Branch
Aerospace Propulsion Division

May 2010
Final Report

AIR FORCE RESEARCH LABORATORY
PROPULSION DIRECTORATE
WRIGHT-PATTERSON AIR FORCE BASE, OH 45433-7251
AIR FORCE MATERIEL COMMAND
UNITED STATES AIR FORCE

NOTICE AND SIGNATURE PAGE

Using Government drawings, specifications, or other data included in this document for any purpose other than Government procurement does not in any way obligate the U.S. Government. The fact that the Government formulated or supplied the drawings, specifications, or other data does not license the holder or any other person or corporation; or convey any rights or permission to manufacture, use, or sell any patented invention that may relate to them.

This report was cleared for public release by the USAF 88th Air Base Wing (88 ABW) Public Affairs Office (PAO) and is available to the general public, including foreign nationals. Copies may be obtained from the Defense Technical Information Center (DTIC) (http://www.dtic.mil).

AFRL-RZ-WP-TR-2010-2146 HAS BEEN REVIEWED AND IS APPROVED FOR PUBLICATION IN ACCORDANCE WITH ASSIGNED DISTRIBUTION STATEMENT.

*//Signature//

MARK HAGENMAIER, DR-III
Sr. Aerospace Engineer, Propulsion Branch

//Signature//

DAVID E. PRITCHARD, Maj, USAF
Chief, Propulsion Branch

*//Signature//

ROBERT MERCIER, DR-IV
Deputy for Technology
Propulsion Directorate

This report is published in the interest of scientific and technical information exchange and its publication does not constitute the Government's approval or disapproval of its ideas or findings.

*Disseminated copies will show "//Signature//" stamped or typed above the signature blocks.

REPORT DOCUMENTATION PAGE

Form Approved
OMB No. 0704-0188

1. REPORT DATE *(DD-MM-YY)*	2. REPORT TYPE	3. DATES COVERED *(From - To)*
May 2010	Final	01 September 2006 – 10 May 2010

4. TITLE AND SUBTITLE
PROGRESS IN APPLYING TUNABLE DIODE LASER ABSORPTION SPECTROSCOPY TO SCRAMJET ISOLATORS AND COMBUSTORS

5a. CONTRACT NUMBER
IN HOUSE

5b. GRANT NUMBER

5c. PROGRAM ELEMENT NUMBER
61102F

6. AUTHOR(S)
Michael S. Brown, Skip Williams, Chadwick D. Lindstrom, and Dominic L. Barone

5d. PROJECT NUMBER
2308

5e. TASK NUMBER
AI

5f. WORK UNIT NUMBER
2308AI01

7. PERFORMING ORGANIZATION NAME(S) AND ADDRESS(ES)

Propulsion Sciences Branch (AFRL/RZAS)
Aerospace Propulsion Division
Air Force Research Laboratory, Propulsion Directorate
Wright-Patterson Air Force Base, OH 45433-7251
Air Force Materiel Command
United States Air Force

8. PERFORMING ORGANIZATION REPORT NUMBER
AFRL-RZ-WP-TR-2010-2146

9. SPONSORING/MONITORING AGENCY NAME(S) AND ADDRESS(ES)

Air Force Research Laboratory
Propulsion Directorate
Wright-Patterson Air Force Base, OH 45433-7251
Air Force Materiel Command
United States Air Force

10. SPONSORING/MONITORING AGENCY ACRONYM(S)
AFRL/RZAS

11. SPONSORING/MONITORING AGENCY REPORT NUMBER(S)
AFRL-RZ-WP-TR-2010-2146

12. DISTRIBUTION/AVAILABILITY STATEMENT
Approved for public release; distribution unlimited.

13. SUPPLEMENTARY NOTES
PAO Case Number: 88 ABW-2010-2713; Clearance Date: 19 May 2010. Paper contains color.

14. ABSTRACT
Development of advanced propulsion systems of interest to the Air Force requires study of the harsh physical environments associated with reacting flows characterized by extremes in temperature and pressure and composition in the case of plasmas. Such environments are difficult to study in detail with methods that make use of physical intrusion into the local environment. Such difficulties motivate the use of noncontact means of study such as optical approaches. By taking advantage of impressive advances in diode laser and associated technology, tunable diode laser absorption spectroscopy (TDLAS) has become a widespread tool for optical diagnostics in reacting flows. Measurements of target species concentration, temperature, pressure, and velocity have been demonstrated in a wide variety of environments by several research groups. Commercialization of niche measurement instruments based on TDLAS has been achieved. The current maturity of the technique enables its application to hypersonic flow paths -- scramjet engines in particular. In this report we summarize our progress in applying TDLAS to scramjet isolators and combustors.

15. SUBJECT TERMS
diode laser spectroscopy, supersonic combustion, optical diagnostics

16. SECURITY CLASSIFICATION OF:			17. LIMITATION OF ABSTRACT:	18. NUMBER OF PAGES	19a. NAME OF RESPONSIBLE PERSON (Monitor)
a. REPORT	b. ABSTRACT	c. THIS PAGE			Mark A. Hagenmaier
Unclassified	Unclassified	Unclassified	SAR	42	19b. TELEPHONE NUMBER *(Include Area Code)* N/A

Standard Form 298 (Rev. 8-98)
Prescribed by ANSI Std. Z39-18

TABLE OF CONTENTS

LIST OF FIGURES

LIST OF TABLES

1.0 SUMMARY

Development of advanced propulsion systems of interest to the Air Force requires study of the harsh physical environments associated with reacting flows characterized by extremes in temperature and pressure and composition in the case of plasmas. Such environments are difficult to study in detail with methods that make use of physical intrusion into the local environment. Such difficulties motivate the use of non-contact means of study such as optical approaches.

By taking advantage of impressive advances in diode laser and associated technology, tunable diode laser absorption spectroscopy (TDLAS) has become a widespread tool for optical diagnostics in reacting flows. Measurements of target species concentration, temperature, pressure, and velocity have been demonstrated in a wide variety of environments by several research groups. Commercialization of niche measurement instruments based on TDLAS has been achieved. The current maturity of the technique enables its application to hypersonic flow paths – scramjet engines in particular. In this report we summarize our progress in applying TDLAS to scramjet isolators and combustors. We also perform close scrutiny of collected signals to ascertain expectations of accuracy and precision in measurements coupled to reacting flows. We examine some TDLAS data sets in this context and discuss the propagation of uncertainties from primary measured values of signal amplitude versus time to secondary values of temperature, number density, and pressure.

2.0 INTRODUCTION

Application of tunable diode laser absorption spectroscopy (TDLAS) to reacting flows has been repeatedly demonstrated in various environments primarily for temperature determination.[1] At least one study demonstrated system control using TDLAS-based measurement input in real time. In this work, closed-loop temperature-based control of a pulsed incinerator was achieved by maximizing the measured time-averaged temperature through adjustment of the phase between primary and secondary air forcing.[2] Overall, the TDLAS technique has matured to the point that several companies including Zolo Technologies Inc., Southwest Sciences, Inc., Los Gatos Research, Inc., and Physical Sciences Inc. have delivered TDLAS-based commercial products for niche measurement applications. In-stream measurements of temperature, pressure, species concentration and velocity are possible in hypersonic reacting flows using TDLAS.[1] Specifically, demonstration measurements of temperature and water concentration have been made at the exit of a direct-connect model scramjet engine,[3] and air velocity has been measured in a direct-connect isolator using water and oxygen absorption.[4] Measurements of temperature and water concentration have also been reported in wind-tunnel testing of model scramjet engines.[5] More recently, spatial information about the shock train in a scramjet isolator has been captured using multiple TDLAS lines of sight and a cluster math algorithm approach to

tomography.[6] These results are all highly encouraging and point toward successful integration of the technique into ground and flight tests. The Hypersonic International Flight Research Experimentation (HIFiRE) program has embraced TDLAS technology. The Flight 1 payload includes two oxygen-based instruments for mass capture determination. And, water-based measurements of concentration, temperature, and pressure, will be executed on Flight 2 using 8 lines of sight at the exit plane of the combustor.

A multiple line-of-sight tunable diode laser absorption system for measuring shock train structure inside a model scramjet isolator at the Wright-Patterson AFB Propulsion Directorate's research cell 18 supersonic combustion facility is described. Multiple rovibrational lines of water are probed using time-multiplexing of multiple diode lasers along 16 lines-of-sight that are projected across a rectangular isolator duct. Static temperatures and water concentration (path-averaged) are computed from a Boltzmann plot for the multiple lines that are measured, and static pressures are determined from the absorption linewidth. The experimental setup and measurement technique are presented here along with the Mach 2 flow (no shock train) results. The absorption measurements agree to within 2% of sidewall pressure transducer measurements and calculated (path-averaged) static temperatures.

3.0 METHODS

3.1 Measurement Technique

Because of the ubiquity of the use of absorption spectroscopy in multiple fields, many different notations are used to describe the same phenomenon.[7,8,9] For clarification, the particular formulation used here is described briefly below and follows of that defined in the HITRAN database.[10,11]

Beer's Law describes the attenuation of light as it passes through an absorbing medium:[7]

$$I = I_0 e^{-\sigma_\nu \Delta N L} = I_0 e^{-\alpha_\nu L} \rightarrow \ln\left(\frac{I_0}{I}\right) = A_\nu = \alpha_\nu L \qquad (1)$$

In Equation 1, I is the transmitted laser intensity through the medium, I_0 is the initial intensity, σ_ν is the absorption cross section at the frequency ν, ΔN is the difference between upper and lower state quantum state densities taking into account degeneracy factors (total quantum state fractional population times the total species density), L is the path length through the absorbing medium, and α_ν is the absorption coefficient at the frequency ν. The absorbance, A_ν, shown in equation 1 is plotted in this report rather than the actual intensity. This is done by dividing through with a reference signal that is recorded in addition to the measurement paths. However, Equation 1 is not in a convenient form for comparison with what is typically tabulated in spectroscopy databases such as HITRAN.[11] These databases replace the absorption cross section

with the line intensity, $S(T)$, and a lineshape function $g(\nu-\nu_{10})$ that describes the spectral lineshape where ν_{10} is the peak center. In addition, the line intensity also incorporates a Boltzmann factor that accounts for the thermal populations of the rovibrational states involved in the transition which is the reason for it being a function of temperature. With these changes Beer's law becomes:

$$I = I_0 e^{-S(T)g(\nu-\nu_{10})N_T L} \rightarrow A_\nu = S(T)g(\nu-\nu_{10})N_T L \tag{2}$$

where N_T is the total density of the absorbing species. The lineshape function is normalized such that integration over frequency or wavenumber yields a value of unity. The data here can be described by a Voigt lineshape function which takes into account the collisional broadening and the Doppler broadening through the convolution of a Gaussian with a Lorentzian.[7] It is computed through the use of the Humlíček algorithm.[12] This means that if Equation 2 is integrated over frequency then the frequency integrated absorption is related to the line intensity and the column density ($N_T L$) through the following relation:

$$\int_{-\infty}^{\infty} A_\nu d\nu = A = S(T)N_T L = \tilde{\alpha}L \tag{3}$$

where the frequency integrated absorbance, A, and the frequency integrated absorption coefficient, $\tilde{\alpha}$, have been introduced. The frequency integrated absorption coefficient has been introduced because it makes description of inhomogeneous flow fields particularly simple. In that case, the frequency integrated absorbance is given by:

$$A = \int_{path} \tilde{\alpha}(l)dl \tag{4}$$

This is an innocuously looking formula that can actually be very difficult to compute because, with the adoption of the HITRAN line strength in Equation 3, $\tilde{\alpha}$, is a complicated function of temperature and pressure. For example, if significant variations in the lineshape occur because of variations in absorbing species temperature, density, and total density then computation of A will require more than a single Voigt lineshape to fit the absorption peak.[13,14] This is found not to be problem when examining the isolator data based on the fit residuals. Another obvious aspect is that if local flow information is desired then it becomes necessary to use some form of tomographic inversion or flow field model to help determine $\tilde{\alpha}$.[13,15-19] For the isolator experiments, CFD simulations are used to compute the frequency integrated absorption that can then be used to compare the simulations with the measurements. This is done in two steps: (1) an image or map of the frequency integrated absorption coefficient is generated from the temperature and densities computed by CFD, and (2) the path integration is done numerically using a trapezoidal integration routine. Then the frequency integrated absorption for each absorption feature can then be input into the routine for computing the temperature and species concentration from a Boltzmann plot. This allows direct comparisons between the CFD and path integrated measurements to be made.

3.2 Spectral Line Parameters and Sample Spectra

Water vapor has several strong rovibrational spectroscopic transitions from the visible to the mid-IR. The availability of compact, spectroscopic quality lasers at telecom wavelengths, 1250-1650 nm, have made the 2 ν_1, 2 ν_3, and $\nu_1+\nu_3$ vibrational bands particularly attractive for diagnostic applications. The abundance of water vapor as a primary combustion product and the relatively large line strengths for these transitions enable these transitions to be used with good sensitivity for many applications.

Single mode, fiber-coupled, DFB lasers are used to generate near-infrared radiation to measure H_2O line intensities in the spectral regions 7184.2-7186.4 cm^{-1}, 7159.5-7161.5 cm^{-1}, and 7179.5-7181.8 cm^{-1}. Principally, P and Q branch transitions of the $\nu_1+\nu_3$ band have been used in this study as identified by the lowercase letters in figure 1. The data was taken during time when the isolator was not back pressured. As can be seen in the figure, peaks *a-d* are quite strong and they are used to determine the temperature and water concentration in the isolator. Peak *a* is also used to determine the static pressure in the isolator. An additional side peak is close to feature c but the one at 7181.15 cm^{-1} is much stronger. Additionally, this side peak shares the same initial state with peak d so its area can easily be subtracted from the peak integration. Finally, peaks e-f have much higher initial state energies and so are only used for much higher temperatures. The data quality of the time-averaged data is excellent as shown in Figure 1 with the residuals being less than 1% of the maximum peak amplitude when using a multi-peak fit Voigt algorithm. Here the raw data is initially divided by the reference beam measurement after both have been appropriately scaled to match in the regions outside of the absorption peaks. Then a cubic polynomial plus Voigt peaks are fit to the resulting spectrum. The cubic polynomial corrects for any nonlinearity that is present as the laser rapidly scans across the spectral region.

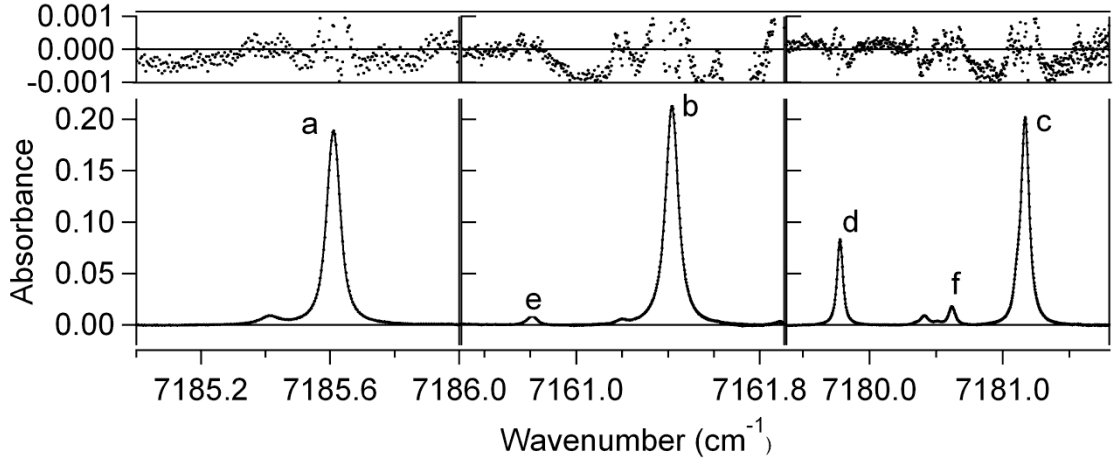

Figure 1: Time averaged (200 averages) spectra, fit, and residuals for the three spectral regions during run AC (see Table 3)

The line parameters are taken from the HITRAN 2004 database and are listed in Table 1. The line intensities at different temperatures are derived using the same procedures and partition

function expressions as defined in HITRAN.[11] Here the line parameters have been taken from the HITRAN 2004 database because it is the most complete source and it compares well to recent studies.[20,21] Some of these transitions have been studied by several authors, and the variation among them is between 2-5% depending on the parameter.[11,20-23] In this study, the HITRAN parameters are used which means systematic errors less than 5% may be present in the following analysis based on these line parameters.[21] It is possible to reduce the systematic error through careful self-calibration of the system over the temperature and pressure range of interest, however, this was not done here because it requires a special setup.

Table 1: Spectroscopic Parameters of Water Lines Used in Study

λ (nm)	ν_{10} (cm^{-1})	S at 296 K (cm^{-1}/molecule-cm^{-2})	E" (cm^{-1})	[ν_1',ν_2',ν_3']	J'Ka'Kc'	J"Ka"Kc"	Label
1391.67	7185.60	7.947e-22	1045.06	1 0 1	6 6 0	6 6 1	a
1396.37	7161.41	1.174e-20	224.84	1 0 1	3 1 3	4 1 4	b
1392.53	7181.16	1.505e-20	136.76	1 0 1	2 0 2	3 0 3	c
1392.81	7179.75	2.299e-22	1216.19	1 0 1	7 6 2	7 6 1	d
1396.49	7160.81	5.406e-24	1874.97	1 0 1	10 6 4	10 6 5	e
1392.64	7180.61	3.038e-23	1477.30	1 0 1	9 5 5	9 5 4	f
1392.55	7181.10	6.858e-23	1216.19	1 2 0	7 7 0	7 6 1	c'

3.3 Determination of Temperature from a Boltzmann Plot

The determination of path averaged static temperature is accomplished by measuring multiple absorption features of the same molecule. The frequency integrated absorption is normalized by the cross section and degeneracy factor for each transition and then plotted versus the initial state energy divided by k_B. In terms of the line intensity above, this results in the following relationship:

$$\ln\left(\frac{A}{S_{ref}}e^{-E''/k_BT_{ref}}\left(1-e^{-h\nu_{10}/k_BT_{ref}}\right)\right)=-\frac{E''}{k_BT}+\ln\left(\frac{Q(T_{ref})}{Q(T)}N_TL\right)+\ln(1-e^{-h\nu_{10}/k_BT}) \qquad (5)$$

where $Q(T)$ is the partition function for the absorbing species and E'' is the initial state energy. At the temperatures and transition frequencies studied here the stimulated emission terms can be ignored (i.e. $e^{-h\nu_{10}/KT}\approx 0$). Figure 2 shows a typical Boltzmann plot for the Mach 2 flow (no shock) taken during run condition AB. Here four water transitions are used to compute the path integrated temperature. The curve shows excellent linearity which is indicative of an early uniform temperature distribution. The slope of the curve is inversely proportional to temperature and can be directly determined from the linear fit. In contrast, the partition function[11] must be

used to determine the species concentration either from the slope of the curve or through using the measured temperature and the frequency integrated absorption of one of the transitions.

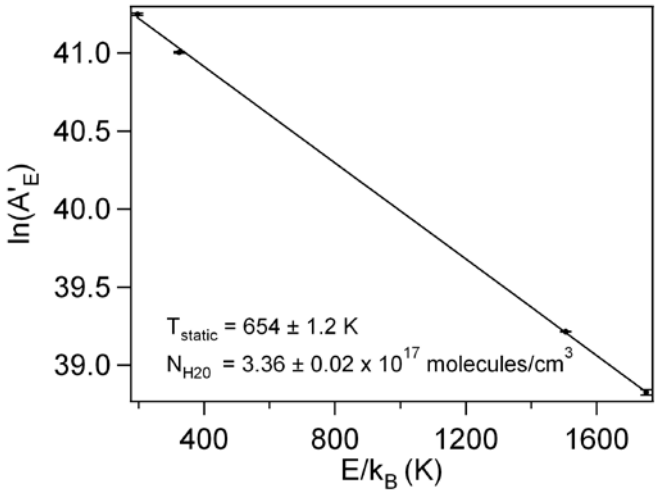

Figure 2: Boltzmann plot for Run AC using the LOS average data from a single beam path. The error bars are standard errors derived from the curve fitting procedure and do not include errors associated with spatial variations in the flow as well as the effect of systematic errors in the line parameters.

3.4 Determination of Pressure from Line Width

Static pressure can be determined from the collisional broadening of the absorption line. The width of the peak is proportional to two factors. The first factor is Doppler broadening which occurs because the thermal distribution of the velocity of the molecules in the gas. This is independent of the states involved in the transition and takes the form of a Gaussian lineshape with a half width at half maximum (HWHM) of:

$$\gamma_D = 3.5812 \times 10^{-7} \nu_0 \sqrt{\frac{T}{M}} \tag{6}$$

where ν_0, the transistion frequency, is given in wavenumbers, T is the gas temperature in K, and M is the molecular mass in grams/mole. At the temperatures in the isolator (400-650 K), γ_D ranges from 0.012 – 0.015 cm^{-1} for lines such as the 7185.6 cm^{-1} feature which is of the same magnitude as the collisional broadening. It is therefore desirable to first estimate the temperature using the Boltzmann plot and fix γ_D. This allows the determination of the collisional broadening from the Voigt fit with a fixed Doppler broadening width determined form the Boltzmann analysis.

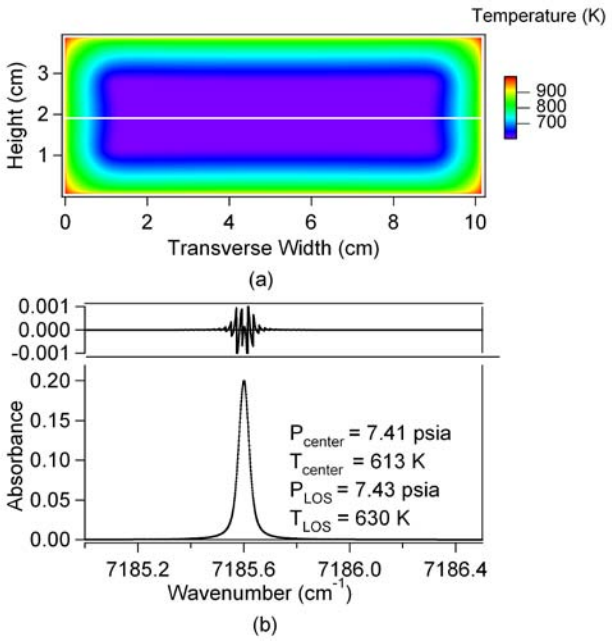

Figure 3. (a) 2D CFD temperature profile in the isolator (flow direction is out of the page) for run condition AC as well as the LOS that is being used to calculate the path averaged measurement (b) CFD simulated lineshape, curvefit to a single Voigt profile and residuals, and the LOS pressure and temperature from the fit compared to the pressure and temperature at the centerline of the isolator.

An important consideration when determining pressure in the manner described above is the approximation of the absorption line by a single Voigt peak. In reality, in the case of Mach 2 duct flow (no shock) the temperature and density change near the sidewall due to the boundary layer with only slight variations occurring in pressure (on the order of 1%). In the presence of shock structure, it is necessary to validate the appropriateness of using a single Voigt profile with significant pressure, temperature, and density inhomogenities along the LOS. In severe cases, the lineshape should be represented as a superposition of Voigt profiles. To assess the effect of the approximation here, simulations have been conducted using the results of CFD (Reference 6 addresses how the CFD flow simulations were calculated). In figure 3, the upper plot shows a pseudo-color plot of the temperature for a vertical cross section of the isolator duct. As can be seen here, there is a temperature gradient of approximately 200 K through the boundary layer. Because of this temperature gradient, the path integrated temperature is higher (630 K) than the temperature at the centerline of the duct which is 613 K. Despite the temperature gradient and the subsequent density gradient (pressure gradients are small here ~ 1%), the single line Voigt does an excellent job fitting the composite lineshape as indicated by the residuals in this figure. The oscillations in the residuals is the result of trying to fit a composite lineshape with a single Voigt as described elsewhere.[14] Perhaps, the most significant aspect of the plot though is the excellent agreement between the static pressure determined from the fit and the static pressure at the duct centerline. This shows that the boundary layer effects on the current static pressure measurements should be minimal for the Mach 2 flow.

Collisional broadening is dependent on the gas molecules involved in the collisions as well as their quantum states. This dependence necessitates the use of different Lorentzian broadening parameters for each transition, and these parameters must be determined for each type of collision partner over the relevant range of conditions for the gas mixture being probed. A molar based addition of the broadening coefficients for a given temperature yields the total collisional broadening coefficient, γ_L. For the vitiated gas mixture present in the isolator, the collisional broadening coefficient, γ_L, is defined in equation 7 as

$$\gamma_L = \chi_{H_2O}\gamma_{H_2)-H_2O}\left(\frac{T_{ref}}{T}\right)^{n_{H20}} + \chi_{N_2}\gamma_{N_2-H_2O}\left(\frac{T_{ref}}{T}\right)^{n_{N2}} + \chi_{O_2}\gamma_{O_2-H_2O}\left(\frac{T_{ref}}{T}\right)^{n_{O2}} + \chi_{CO_2}\gamma_{CO_2-H_2O}\left(\frac{T_{ref}}{T}\right)^{n_{CO2}} \quad (7)$$

where χ is the mole fraction of the particular species and the species specific broadening coefficients for the major flow constituents are used, T_{ref} is the reference temperature (296 K here), T is the gas temperature, and n is the temperature coefficient. The particular mole fraction of the major flow constituents is determined from calibrated mass flow and the measured >99.9% combustion efficiency of the burner. Because four broadening coefficients and temperature coefficients are required, it is difficult to find a single literature source that has a complete set. The computational work of Delaye et. al[24] lists the required quantities. However, as pointed out by Nagali et. al[25] the temperature coefficients can have significant error for the 7185.6 cm^{-1} line. The self-broadening coefficient of H_2O found in the work of Nagali et al disagrees with a more recent measurement of Lepere, et al.[22] In addition, neither experimental author reports a temperature coefficient for the oxygen line broadening parameter. These disagreements though are not uncommon and a critical although somewhat dated review of problems associated with collisional broadening parameters for water vapor lines is given in the work of Gamache, et al.[26] As stated therein disagreements within line parameters typically can lead to variations in estimated pressure on the order of 10%. Here the most current line broadening parameters from the literature sources cited above and a recent study by Durry, et al[20] of N_2 and O_2 broadening are combined. The line parameters for the 7185.6 cm^{-1} line used in this study are listed in Table 2.

Table 2: Broadening Parameters and Temperature Coefficients for line *a* (7185.6 cm^{-1})

Perturbing Species	γ at 296 K (cm^{-1} atm^{-1})	Temperature Coefficient n
H_2O	0.23 [31]	0.56 [33]
N_2	0.0456 [18]	0.64 [33]
O_2	0.0271 [18]	0.49 [17]
CO_2	0.086 [33]	0.74 [33]

4.0 DISCUSSION OF RESULTS

4.1 Measurements in an Isolator

In this study, the static pressure, temperature, and density fluctuations in a supersonic shock train of a model scramjet isolator is explored using a TDLAS sensor based on 16 LOS. This particular problem has been chosen for several reasons. Significant interest exists in the development of air mass-flux or mass-flow sensors for in-flight measurements based on TDLAS technology for aerospace applications. Although excellent measurement accuracy to the level of 1% has been previously reported for low speed flows, the conditions found in scramjet isolators pose significant new challenges. The flow is typically turbulent because of the high Reynolds numbers and shock structures can be present in the flow based on the engine operating conditions in addition to the problems of boundary layer effects. By combining 14 LOS with 2 diagonal LOS for velocity measurements it is possible to begin to develop an understanding of the influence shock trains on mass-flux measurements although this will not be the current focus of the two part series. Instead the interest is on the structure of the shock train itself. Much is known about supersonic shock trains in ducts which result from the interaction of shocks with the boundary layer. In a supersonic shock train, a sequence of shocks forms in the streamwise direction that depends to a large extent on the Mach number and boundary layer thickness. Although the flow is truly three dimensional in nature, the dominant variations occur in streamwise direction and so significant information about the shock train structure can be obtained through probing that direction of the flow. This simplified the experimental setup considerably and allowed tests to be conducted with existing optical access hardware. In the future, it should be possible to extend these measurements by probing the transverse direction as well at the cost of a more complex setup. Much information has been obtained using wall measurements of this phenomena but is limited to determining the shock front location and much less information exists about shock train inflow properties as well shock train dynamics. Here the goal is to obtain time dependent inflow data (1 kHz) at several spatial locations along the flow direction that can be compared to theory as well as computational fluid dynamics (CFD) simulations. Traditionally these flow properties have been explored using particle velocimetry techniques, high-speed Schlieren, and in-stream pressure probes. These studies though focused on slower flows (M~1.6) than the ones studied here (M~2.2) where the shock train unsteadiness was much less and the shock train was known to be a normal shock train. The use of TDLAS can complement these measurements, and it offers the significant advantage that it can be miniaturized so that in-flight measurements could be possible in addition to ground testing.

In this report, the system design, measurement technique and Mach 2 flow results will be presented. This allows comparison of system performance to previous measurements that have been made in the literature as well as to conventional pressure transducers and thermocouples. Also introduced here is the use of collisional broadening to measure the static pressure in a supersonic flow. Although collisional broadening has been well known since the beginning of spectroscopic techniques, to our knowledge it has not been exploited in the measurement of supersonic flows. Probably the most significant reason for this is that previous campaigns have not been interested in flows with substantial pressure variations. However, there is also the issue

of accurately knowing the line broadening parameters which are continually improving with more accurate measurements and calculations being made.[11] Here it will be shown that accurate measurements of pressure can be made if the line parameters are well known.

4.1.1 Optical Layout and Control/Acquisition Electronics

Figure 5 shows a schematic of the common optical components used in each experimental setup. Three distributed feedback diode lasers (NEL NLK1E5GAAA) all operating in a different spectral region are time-multiplexed in a single period lasting 1 millisecond and combined using a 1x4 combiner (Newport F-CPL-B14350). The combined beam is then split using a 10/90 splitter (Newport F-CPL-B12351) with the 10% beam going to a 50/50 splitter (Newport F-CPL-B12355) whose output is routed to either a SiO_2 (Los Gatos Research) etalon with a 2.000±0.002 GHz @ 1550 nm free spectral range that monitors the frequency spectrum of the lasers or to a photodetector (Thorlabs PDA 400) that is used as a reference. The remaining 90% of the beam enters another 50/50 splitter that then connects to two 1x8 fiber optic splitters (Newport F-CPL-1x8-OPT) that are then collimated (Thorlabs F240APC-C 8mm FL). The signal is attenuated by a factor of -18.5 dB as it passes through the splitters and ultimately each LOS will see an average power of 280 μW if the average input power of the lasers is 20 mW. This power level allows excellent signal to noise with the detector arrays as can be seen in figure 1. The collimators are mounted on a precision drilled baseplate to enable tight beam placement. Because of the physical limitations of the optical mounts, the spacing of the collimator arrays is slightly larger than the 3" photodiode array used for detection.

The raw transmitted laser power is measured simultaneously on all 16 paths through the use of in-house custom designed InGaAs photodiode arrays. These custom designed arrays amplify the signal from 2mm diameter FGA21 photodiodes (FGA 21 from ThorLabs) using a Texas Instruments OPA380 transimpedance amplifier/op amp for each photodiode. This amplifier with 90 MHz of gain bandwidth is a single supply (+5 V) and therefore requires a bias be applied to the photodiode so that input voltages are not driving to 0 V. The simplified schematic of the optical amplifier circuit is shown in Figure 5. Several design tradeoffs were made in the circuit design to allow for an easily scalable system as well as ease of use. A 256 tap, 200 kΩ digital potentiometer (AD5262) allows for the gain to be controlled digitally. The leads to an additional 25 pF of parasitic capacitance that decreases the bandwidth and combined with the photodiode junction capacitance of 500 pF at 0 bias voltage (at 0.5 V bias it is less) yields a total input capacitance of 525 pF. This capacitance with gain setting of 30 kΩ results in an overall bandwidth of approximately 950 kHz as determined from the manufacturer's datasheet. At 200 kΩ the bandwidth of the circuit will decrease to 370 kHz. Although this seems considerably faster than the 1 kHz scan rate the primary issue is the scan time across the peak which here is approximately 5.6 μS. The frequency response must be faster in order to get a correct peak shape and area which is the case here for the nominal 30 kΩ feedback resistor used; however, at high gains this can become a problem. This can be improved by moving to faster amplifiers with a larger gain-bandwidth product. The use of smaller photodiodes are possible as well, however,

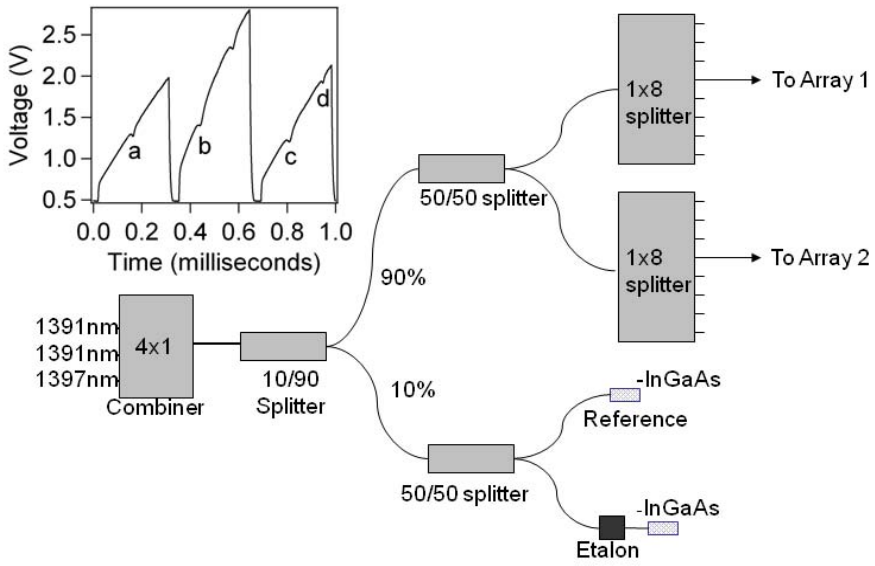

Figure 4: Optical layout of multiplexed diode laser system and time multiplexed signal (inset) with peaks labeled as indicated in Figure 1 and Table 1

noise due to optical turbulence increases as the photodiode area decreases if the beam overfills the detector. So, clearly improvements can be made to these photodiode arrays, however, the signal is still excellent for the size of the measured absorption peaks in Figure 1.

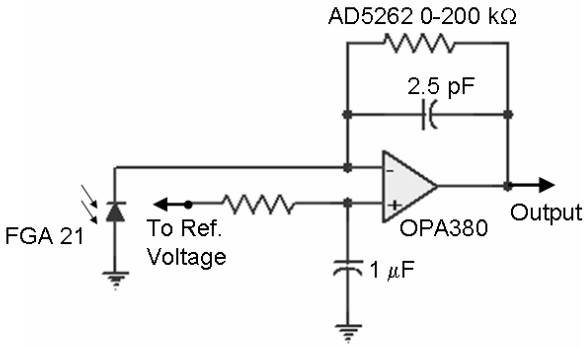

Figure 5: Simplified schematic of the optical amplifier circuit

The signal is then digitized into 14 bits using a NI PXI-6133 (32 MSamples onboard memory) S Series Multifunction Digital Acquisition (DAQ) Device sampling at a rate of 2.5 MSamples/s. The amplifier output as well as all control signals and power are provided through a 68 wire cable that connects directly to the photodiode array using a SCSI-3 type connector. This along with adaptable software written by us allows for easy scalability of the system because each digitizer card and photodiode array provide an additional 8 channels. A PXI chassis is used to hold all of the data acquisition equipment; i.e. computer/controller, DAQ cards, and the function generators used to drive the lasers. Because of the unsteady nature of the shock, a NI Intel Core

Duo 2.0 GHz Processor with 2GB of DDR2 host RAM is used to average 200 spectra, determine peak areas through trapezoidal integration, and then create a real time (1-5 Hz) LOS image along the flow direction. This provided feedback as to the success of the data runs. It also provides control of the current ramp of laser diodes through a National Instruments PXI-5402 function generator. The digitizers and function generators are synchronized to ~ 5 nanoseconds using a 10 MHz backplane clock signal. Because all the channels are all simultaneously sampled at the same time (18x2.5x2 = 90 MB/s), the PCI bus in the PXI chassis cannot sustain continuous data transfer to the hard drive in the current configuration. Instead a short segment of data (0.2 s) is captured, processed, and saved to the hard drive. This process takes approximately 5 s and then another 0.2 s of data is captured, processed, and saved. Although the shock is unsteady it has been found that pushing the shock slowly from the rear of the isolator to the front enabled the key shock features to be measured. The data acquisition/processing software was developed in LabWindows to allow a scalable architecture for developing TDLAS based tomography. The data acquisition rates will vary based on the channel count, however, at least 2 seconds of continuous data can be acquired because of the large on-board memory of the digitizer cards.

4.1.2 Isolator Test Setup

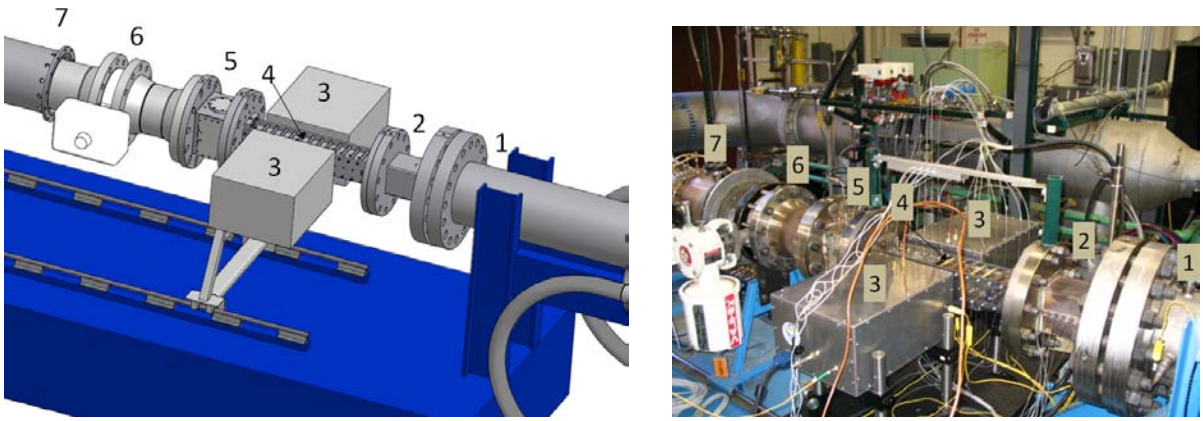

Figure 6. (a) Schematic of the supersonic combustion test facility and (b) photograph of the facility that indicate 1 – burner, 2 – facility nozzle, 3 – TDLAS hardware, 4 – isolator, 5 – extension, 6 – backpressure valve, and 7 – exhaust line

AFRL/RZA owns and operates two direct-connect supersonic combustion facilities. Figure 6 shows a schematic of the Research Cell 18 where the experiments were performed. This facility was designed to allow basic studies of supersonic reacting flows using conventional and non-intrusive diagnostic techniques. It consists of a natural gas fueled burner, transition flange, interchangeable facility nozzle (Mach-1.8 and 2.2 currently available), modular isolator, modular combustor, instrument section and calorimeter. The rig is mounted to a thrust stand

capable of measuring thrust of up to 2000 lbf. The test rig is provided with continuous flow of up to 30 lbm/sec at 750 psia at a temperature of up to 922F, and exhausts into a 3.5 psia continuous flow exhauster system. The facility can simulate flight conditions from Mach 3.5 to Mach 5 at flight dynamic pressures of up to 2000 psf. For the current study, the combustor was removed and replaced with a large valve that was used to simulate the pressure rise associated with combustion. The isolator is fitted with 1" high x 3.4" wide optical access ports designed to hold 1.7 cm (0.68 in) inch thick quartz windows or steel inserts. The quartz windows are wedged at 5º on the outer surface to prevent etaloning. The nozzle and isolator are instrumented with static pressure taps and thermocouple with a frequency response of approximately 10 Hz. No difference in isolator performance has been noted between the using the quartz windows or the thermal barrier coated (TBC) steel inserts despite the differences in surface roughness between the quartz and the TBC. A key enabling aspect provided by this facility is that the vitiation which is used to increase the flow enthalpy to the correct level provides the water vapor being probed in this experiment. Although it is possible to measure oxygen, it is difficult to achieve the excellent signal to noise ratio that can be obtained with water absorption features. This facility has been described in detail elsewhere.[27,28]

Table 3 Average Run Conditions – Facility Nozzle Mach Number = 2.2

Start Time	Incoming Air Temperature (K)	Total Temperature (K)	Total Pressure (psia)	Water mole percent (%)*	Reynolds Number
19:23:07	300	667	50	3.03	9.1×10^5
19:36:21	300	1016	50	6.93	4.6×10^5
21:26:20	589	667	50	1.11	9.1×10^5
21:34:58	589	1016	50	4.94	4.6×10^5

*Assumes dry facility air

In this report, the analysis will focus on four sets of data labeled runs AB, AC, AF, and AG. The burner settings as well as the nozzle Mach number, water molar percent, and the Reynolds number for each case are shown in Table 3. The Reynolds number has been computed using the equivalent duct diameter (5.75 cm) for a rectangular duct with cross section of 3.81 x 10.16 cm. The amount of vitiation used for each run depended on the desired total temperature and whether the air was preheated using electric heaters. The temperature and total pressure showed only a few degrees and about a half a psi variation over the course of a data collection cycle which means that they are accurate to 1% over the course of the test run. The water molar concentration though has to be computed from the mass flows of the compressed natural gas (CNG) and oxygen. In this case, several issues exist. First, CNG is not pure methane but includes CO_2 and larger alkanes such as ethane and propane. The presence of CO_2 will lower the amount of water in the vitiated flow, but the combustion of larger alkanes will increase it. The CNG used in these experiments is composed of 95.19% methane, 2.30% ethane, 1.28% CO_2, 0.65% nitrogen, and 0.58% higher alkanes (propane, butane, pentane, etc.) based on an average of the gas composition reported by the CNG provider.

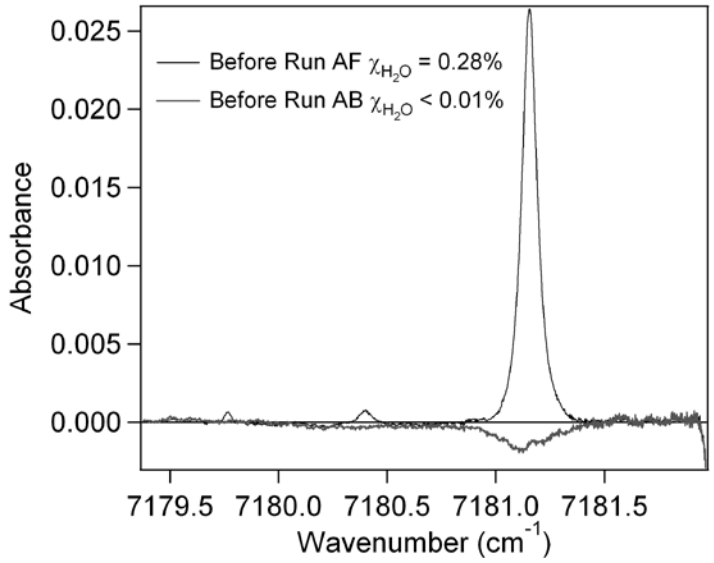

Figure 7. Absorption spectra taken before runs AF and AB with no vitiation to assess the effectiveness of the purge boxes.

Second, in the time-averaged case shown here, a low frequency (~0.05 Hz) 1% oscillation was observed in both mass flow rates of the oxygen and CNG controllers which is averaged out here because the data run usually lasted on the order of 1 ½ minutes – 2 ½ minutes. However, for the comparisons made later a 0.2 s data segment was used and the average water mole percent was computed for that particular time from the mass flow controller data. Finally, variations in the incoming air's moisture content has been observed as can be seen in figure 7 which shows measurements made to assess the effectiveness of the purge boxes. Because the purge boxes do such a good job as evidenced by the apparent negative absorption peak associated with data taken before run AB, it is possible to use the data to assess the water mole percent of the incoming air. Here the negative absorption peak is actually due to a small air path (~ 1-2mm) in the reference signal that is unmatched on the measurement channels most likely due to the air gap between the photodiode and the end of the optical fiber (a Thor-Labs SM1FCA adapter plate is used to connect reference fiber to the PDA 400). Because it is of the order of 0.01-0.03% water molar percent, we ignore it in our calculations. However, as can be seen in figure 7 the data collected before run AF had much greater water content. Here the water concentration of $2.0 \pm 0.1 \times 10^{16}$ molecules/cm^3, the static temperature of 275 ± 15 K, and the static pressure of 4 ± 0.2 psia indicates that the incoming air has a water mole percent of 0.28% ± 0.03%. Although this is a very small water molar percent, it is very important when assessing the ability of the TDLAS to measure the water concentration in the case of run AF where this effect would lead to a 25% error if not corrected.

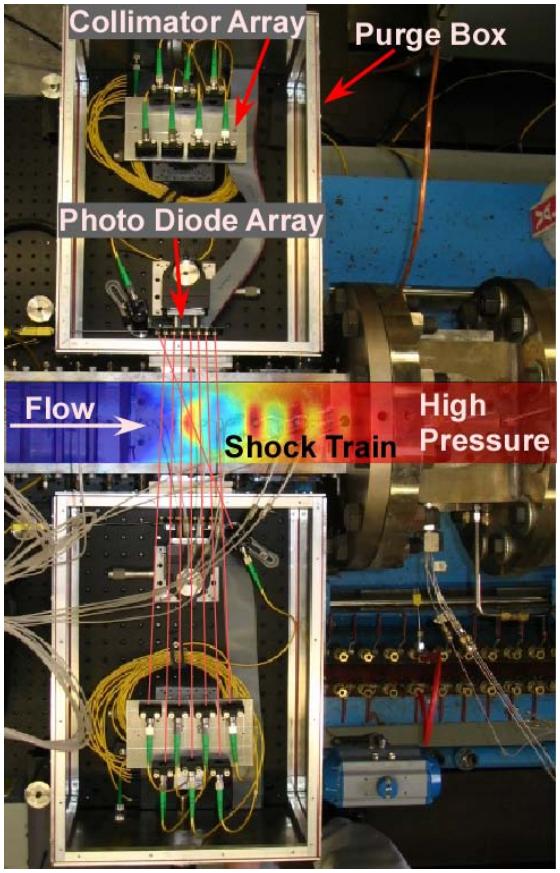

Figure 8. A top view of the experimental setup with an overlay depicting the shock train structure in the isolator is shown. The measurement plane occurs at mid-height in the isolator. For clarity, only 8 beams (red lines) going from the bottom purge box to the top are shown. However, another 8 beams from the top to the bottom box are also used. The indicated flow direction is what will be used in subsequent figures.

Figure 8 shows the experimental layout as implemented during the test campaign. The most significant changes in the flow structure occur in the streamwise direction and consist of high and low regions of density, pressure and temperature in the shock train. It is the goal here to detect these variations in good detail in the streamwise direction with an approximate spacing of the 14 LOS of 5 mm. Obviously, higher aspect that can be seen from the image is the reason for the indicated probing geometry of 14 beams being aligned nearly perpendicular to the flow direction. The most significant changes in the flow structure occur in the streamwise direction and consist of high and low regions of density, pressure and temperature in the shock train. It is the goal here to detect these variations in good detail in the streamwise direction with an approximate spacing of the 14 LOS of 5 mm. Obviously, higher resolution will improve the quality of the data. However, significant aspects of the shock structure can be measured. The photodiode arrays as well as collimator arrays are mounted on standard 12”x18” optical breadboards that are inserted into aluminum purge boxes. These purge boxes were sealed except for inlets and exit ports for N_2 purge gas and a face plate that had a rectangular hole cut into slightly larger than the isolator windows. The front of each box was press fit against a ceramic firebrick cutout that insulated the purge box from the isolator wall that could reach temperatures

of up to 700 -800 K during high-enthalpy runs. Finally, a mask insert that restricted the photodiodes field of view was found necessary for runs AC and AG due to black-body radiation associated with the interior walls of the isolator. The boxes were mounted on a much larger breadboard that was attached to the thrust stand rails that allowed the whole setup to move with the test rig as it thermally expanded. Compressed nitrogen was used to pressurize a LN_2 dewar whose blow off was used to cool and purge the boxes of ambient air. As mentioned previously, excellent purge was achieved and no evidence of water vapor due to the regions outside the flow was observed during the experiments.

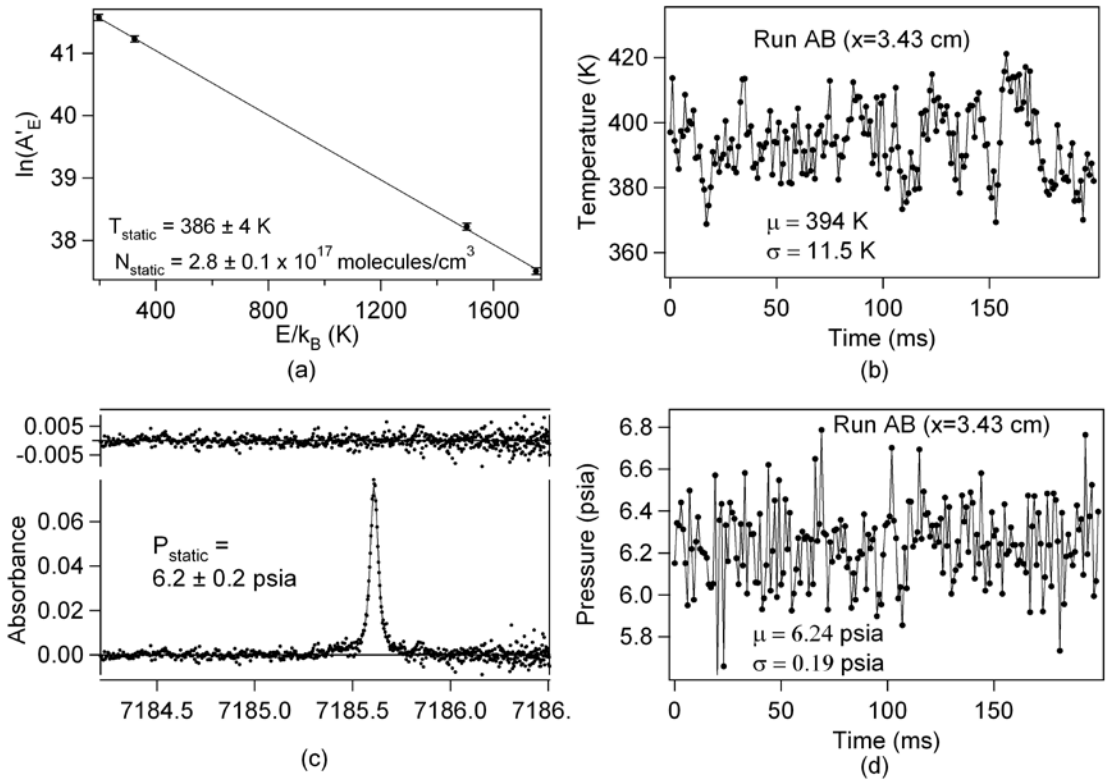

Figure 9 (a) Boltzmann plot for one scan (0.3 ms), (b) temporal variation of temperature versus time, (c) spectrum for one scan, and (d) pressure versus time all for the LOS at x = 3.43 cm from the upstream edge of window

4.2 Discussion of Isolator Measurements

The assessment of the measurement accuracy and precision are necessarily more difficult for the case of the Mach 2 (no-shock) isolator flow than for steady flow problems such as laminar flames which have been studied extensively. Here issues such as having high-quality data that can be used to compare the measurements with, flow unsteadiness, and small spatial variations in the flow field all will impact the accuracy as well as precision of the measurements. In addition, systematic errors due to errors in the spectroscopic parameters will affect the comparison. Nevertheless, as will be shown here excellent comparisons exist between static temperatures and calculations, static pressures and average wall pressure measurements, and the water mole percent and complete combustion assumptions.

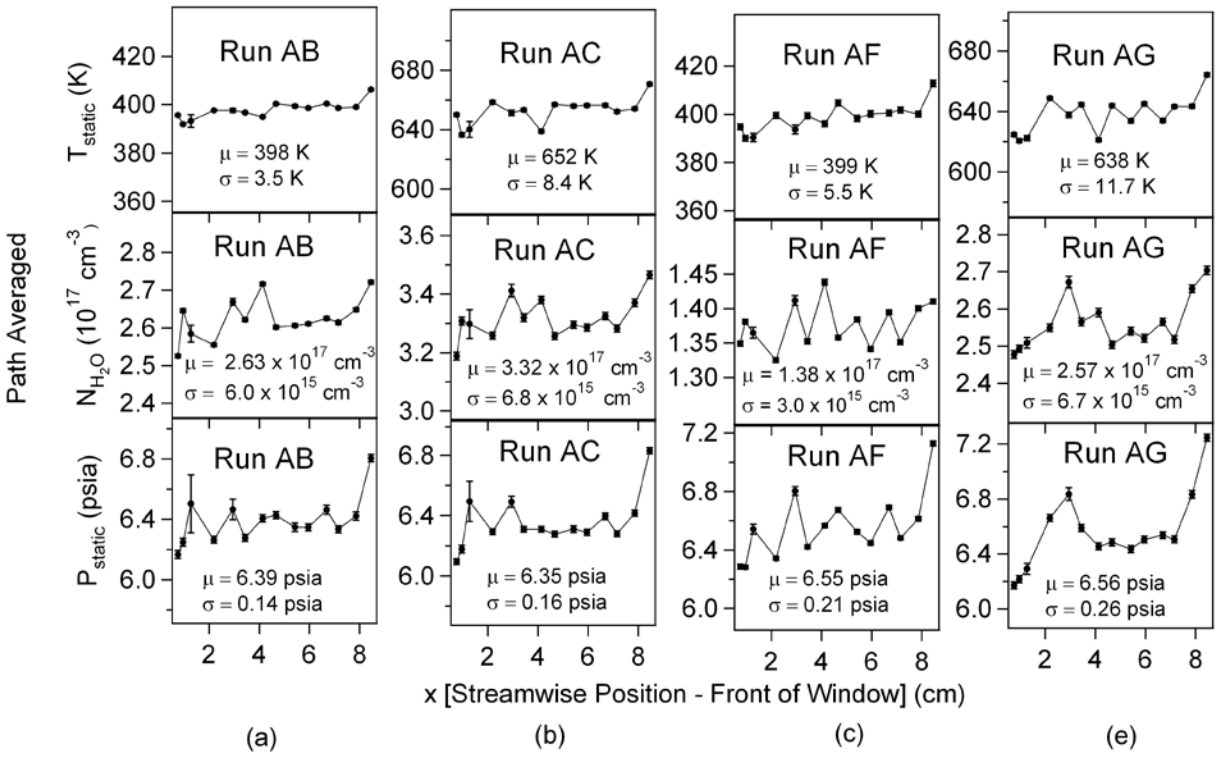

Figure 10 Streamwise variation of time and path averaged static temperature, water concentration, and static pressure for run conditions (a) AB (b) AC (c) AF, and (e) AG. Scales are taken to be ±10% of the mean. The displayed error bars are fit error bars and do not reflect inaccuracies due to line parameters.

Figure 9 shows the measurements for a single LOS located 3.43 cm from the upstream edge of the window during run AB (no backpressure condition). At any given time, the data is of excellent quality and the temperature and water concentration can be deduced from the Boltzmann plot as well as pressure from the linewidth of line *a*. The fluctuations in static temperature and pressure are of the order 3% and reflect variations in the rig operating conditions as well as the baseline estimation procedure used to process the data.

As can be seen in Figure 10, excellent precision is obtained between identical flow conditions despite significant time difference between runs and the use of unheated or preheated air to the burner. Figure 10 also shows how the time averaged, spatially resolved data varies as a function of streamwise position in the duct. The maximum value of the amplitude variations is always less than 10% of the mean value (scale is ±10%) and often much less. The data for this analysis was acquired by first averaging the spectra from the 200 different scans in one data segment. Multi-peak Voigt fits were then used to fit each spectrum in the manner described in section II and obtain the data in figure 10. The data segment was chosen by examining each run time during the course of each run when it was expected that no shock was present in the window. However, in case of Run AG, the very front edge of a shock is beginning to enter the rear of the window as confirmed by an inspection of the isolator pressure taps. All cases show that the LOS closest to the rear of the window exhibits a rise in pressure compared to the other LOS. This also appears to be the case for the pressure tap data although it has a much sparser resolution. It may be the case that a weak shock is attaching near the rear of the window where there is a small break between the window and the TBC coated sidewall of the isolator. The error bars in figure 10 correspond to the standard statistical error bars from a curve fit. These error bars agree with the results reported in Figure 9 because the error in the mean in that case roughly corresponds to the standard error bars in Figure 10. Notice that although standard errors are being reported nothing is being said about confidence intervals. This requires knowledge of the underlying distribution of the data which is difficult to determine and most likely not Gaussian. However, the small standard errors suggest that something other than statistical errors are causing the spatial oscillations such as local flow fluctuations. By averaging over these spatial oscillations an increase in measurement precision is achieved.

Table 4 Static Pressure Comparison

Run	TDLAS (psia)	Pressure Taps (psia)	% Difference [TDLAS-P. Taps]
AB	6.39 ± 0.32	6.59 ± 0.20	-3.0 %
AC	6.35 ± 0.32	6.49 ± 0.09	-2.2 %
AF	6.55 ± 0.33	6.65 ± 0.08	-1.5 %
AG	6.56 ± 0.33	6.58 ± 0.14	-0.3 %

Figure 11 shows that spatial oscillations also exist in the sidewall pressure measurements. As can be seen here during run AC, the pressure fluctuates along the duct. The error bars indicate the calibration error of the pressure transducers so the oscillations that are being observed are due to flow field variations. This should be expected for a turbulent flow. In an effort to eliminate these fluctuations, the three pressure taps that span the window region (1 bottom side and 2 top side) are averaged together and compared to the spatially and temporally averaged TDLAS measurements. The comparison between the TDLAS measurements, pressure tap measurements, and CFD is presented in Table 4. As can be seen in the table, the agreement is

excellent with the worst disagreement being 3% for run AB and the average disagreement being 1.75% between TDLAS and the average pressure tap pressure. This is less than the error bars for the TDLAS measurements which have been taken to be ± 5% (0.32 psia) due to possible systematic errors in the line broadening parameters in accordance with reference 34. The errors for the pressure taps are the standard deviation of the mean of the three pressure taps located within the window region. Note that the TDLAS data shows remarkable similarity between runs AB & AC and runs AF & AG. The statistical precision of the TDLAS data can be determined from figure 10 to be approximately 0.04-0.07 psia so it would be much better than the pressure transducer data which only exhibits a precision of 0.1 – 0.2 psia. At the current level of analysis, though, it will be difficult to determine the sources of these differences because it could be due to a large number of factors involved in accurately determining the facility operating conditions.

The static temperature of the flow can only be compared at the current time to the CFD simulations. In order to do this properly, the path integrated temperature must be determined from the CFD as described in section II part C.

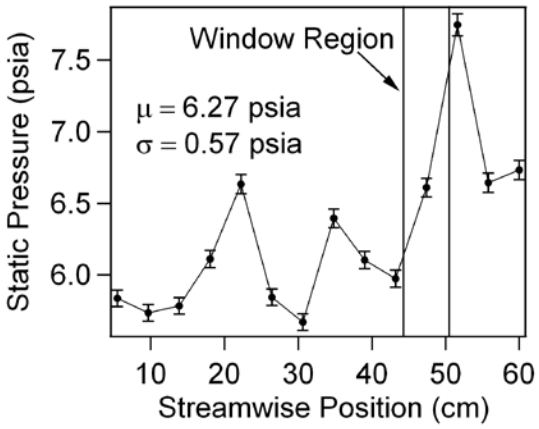

Figure 11. Pressure measurements using conventional static pressure taps on the bottom side of the isolator as well as the window region near the time the Mach 2 flow TDLAS data was taken for run AC.

The comparison is shown in Table 5. As can be seen from this table, excellent agreement is found between the computed temperatures and the measured ones with a maximum difference of 3.3% and an average difference of 2.3%. The error bars have been computed based on a ±3% systematic error plus the statistical error evident in figure 10.

Table 5 also shows the comparison between the facility based computations and the TDLAS computations of water mole percent in the vitiated flow. The TDLAS results for the water mole percent are based off of the TDLAS static pressures in Table 4, TDLAS static temperatures in Table 5, and TDLAS water concentrations. The ideal gas law is used to compute the total densities from the TDLAS static pressure and temperature, and the measurement errors are propagated through using standard methods. The facility computations are based on flow rates through facility provided mass flow controllers that provide the flow rate of air, compressed natural gas, and oxygen to the burner. The molar fraction of water is then computed based on complete combustion of the CNG mixture. Because the CNG is not pure as detailed earlier, the maximum possible error of 8% was been used to determined the errors for the facility

computations. In addition, the measured 0.28 % water mole percent has been added in the computations for runs AF and AG to account for the water present in the facility air. The agreement between the TDLAS and the calculated water mole percent methods is quite good despite the approximations being made with the facility agreeing with the TDLAS computations to the level of 7% except for the case of run AF. There the difference in these measurements is on the order of the facility air correction to the small amount of water produced under those conditions. In general, the agreement is within the error of the facility computations.

Before concluding this section, it is useful to compare the measurements to previous measurement campaigns in similar facilities. In particular, a straightforward comparison with the work of Upschulte, et al. is useful to see how the measurement accuracy and precision have increased. For that particular case, two LOS were used to probe the flow along an 18 cm path which is almost a factor of two longer than the paths used in the current experiments (10.14 cm). In that work, the measured static temperatures were found to agree with the predicted static temperatures within 7-11% which is a factor of 2-3 more than the maximum disagreements observed here. In addition, the water mole percent was observed to differ from the predicted

Table 5 Path Averaged Static Temperature Comparison and Water Mole Percent

Run	Temperature			Water mole percent		
	TDLAS (K)	CFD (K)	% Difference [TDLAS-CFD]	TDLAS (%)	Facility Computation (%)	% Difference [TDLAS-Facility]
AB	398 ± 4	389	2.2 %	3.30 ± 0.20	3.07 ± 0.25	7.32
AC	652 ± 10	630	3.3 %	6.83 ± 0.38	7.09 ± 0.57	-3.7
AF	399 ± 4	389	2.6 %	1.68 ± 0.10	1.44 ± 0.28	17
AG	638 ± 11	630	1.25 %	5.04 ± 0.29	5.27 ± 0.50	-4.4

water fractions by a factor of 17-56% which is a factor of 1-3 more than the maximum disagreement observed in this work. However, as observed here, the lowest disagreements were observed with the highest water concentrations suggesting that approximations used in computing the water fraction were also a factor in that work. Most of the improvement is probably due to the increase in the quality of the optical hardware over the course of the last 8 years as well as more accurate determination of the absorption line parameters. Some of the differences could also be facility improvements. However, it is also the case that the use of multiple paths allows for averaging over spatial inhomogenities that would be more difficult with two lines of sight. The work of Liu, et al. represents a more recent study (2005) of the test rig in research cell 22 and it shows the improvements in optical hardware that have been recently made. It shows many of the improvements in data quality that can be observed by comparing the current study to the one by Upschulte, et al. Unfortunately, no comparisons to the predicted facility vitiation conditions were made so a straightforward comparison cannot be made but it appears that the measurement quality is more in agreement with the results given here. The extent of LOS multiplexing (14 LOS) and data acquisition is new.

The design, setup, and measurement accuracy and precision of a 16 LOS tunable diode laser absorption system has been demonstrated. Also, the first ever measurements of static pressure using linewidth broadening in a scramjet isolator have been reported. The accuracy of the measurements is excellent with average differences from the pressure taps on the order of 2% for static pressure and the temperature agreement with CFD being of the order of 2%. The comparison of water mole percent is more complex and requires that approximations be made in facility computations. Nevertheless, excellent agreement is once again seen with the exception of the run AF ($\chi \sim 1.5\%$) where the disagreement is 17% but is still within the facility error bars. The hardware and software developed for this study pave the way for measurements of shock structures in the isolator. Furthermore, the system described here is scalable and should enable high precision, spatial and spectrally multiplexed TDLAS measurements for supersonic flow characterization, combustion product analysis, and real-time monitoring of the flow environment. At present 16 beam paths are employed, but the system could be readily extended to 128 beam paths with the appropriate optical access. The importance of this advancement is more evident Reference 6 which focuses on the analysis of transient behavior.

4.3 Accuracy and Precision of TDLAS Measurements in Hypersonic Flows

The significant TDLAS measurement achievements noted above point to a general need for understanding, in a detailed way, the accuracy and precision to which TDLAS measurements can be made in reacting flows. While the relative accuracy and precision may vary from one

Table 6 Near-infrared (~1.39 μm) water transitions used in study.

Transition Label	Transition Frequency (cm^{-1})	Lower Energy Level (cm^{-1})	Line Strength at 296 K (cm^2 $molecule^{-1}$ cm^{-1})
A	7161.410	224.838	1.168E-20
B	7179.752	1216.195	2.438E-22
C	7181.156	136.762	1.488E-20
D	7185.597	1045.058	8.335E-22

particular application to another, the limits of both will be dictated by general considerations of signal-to-noise ratios and signal processing algorithms. In applications associated with reacting flows, the largest source of uncertainty is typically the signal-to-noise ratio (SNR). The SNR in turn depends on intrinsic detector noise, A/D bit depth, parasitic etalons, gross beam steering, beam obscuration, etc. Limits of accuracy and precision will also be determined by the accuracy of the fundamental spectroscopic constants associated with the target species and the specific transitions accessed during signal collection. Some of this thinking has been addressed as researchers have sought resonant features that exhibit temperature sensitivity over the anticipated measurement temperature range. We are currently examining such issues in a detailed manner that is independent of hardware details using TDLAS data acquired in a number of flowing

environments. The following discussion is focused on single-scan (un-averaged) water absorption spectra acquired in a time-multiplexed manner over the transitions shown in Table 6. The spectra were acquired using direct absorption and individually processed to determine the integrated area under each spectral feature. Temperature was then derived from the integrated areas using two approaches. In the first, ratios of integrated areas were calculated and equated to the corresponding ratio of the line strengths as shown here

$$\frac{A_1}{A_2} = \frac{LS_1}{LS_2} \tag{8}$$

The line strengths themselves are known functions of temperature and the ratio of two is simply given by

$$\frac{LS_1}{LS_2} = \frac{LS_1(T_o)}{LS_2(T_o)} \; e^{-\frac{1}{k}(E_1 - E_2)\left(\frac{1}{T} - \frac{1}{T_o}\right)} \tag{9}$$

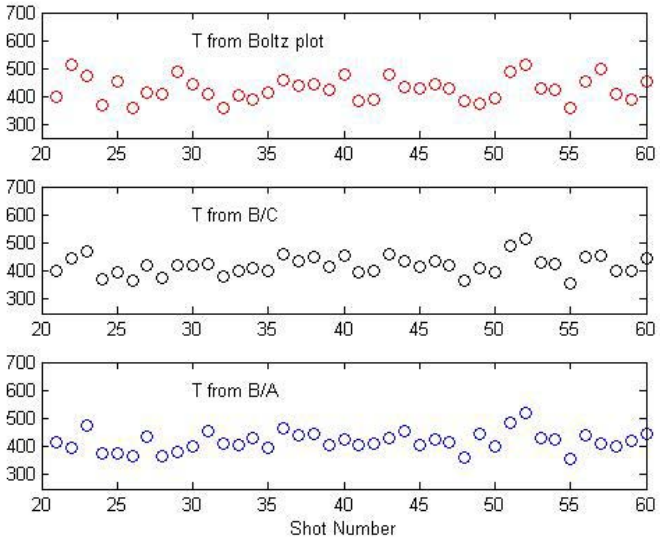

Figure 12. Single-shot TDLAS-based temperature measurements (T in K) acquired in a Mach 1.8 flow stream at the entrance to the isolator.

where E_i denotes the lower energy of the i^{th} transition and T_o a reference temperature (296 K). Extracting a temperature value from the line ratio method is simply a matter of finding the unique value for T that satisfies Eqn. 8 and 9. (The line strengths at the reference temperature are found in the open literature.) The second approach for determining the temperature is based on the well-known Boltzmann plot. In this prescription, the logarithm of the integrated areas

normalized by their corresponding lines strengths at the reference temperature are graphed as a function of the corresponding values of the lower-state energy level for the transitions. A linear, least-squares fit to the plotted data yields both the temperature and density as seen from Eqn. A5 in the Appendix. The derived density (N) associated with the first approach is found directly from $A_1 = LS_1(T)\,N\,L$ using the temperature as found from Eqn. 8 and Eqn. 9. The anticipated numerical uncertainties associated with the derived temperatures and densities associated with both approaches are written explicitly in the Appendix. Both approaches presume local thermodynamic equilibrium of the target species over the time duration of the acquisition of a single spectrum. This assumption is sound under the conditions that the data presented here were

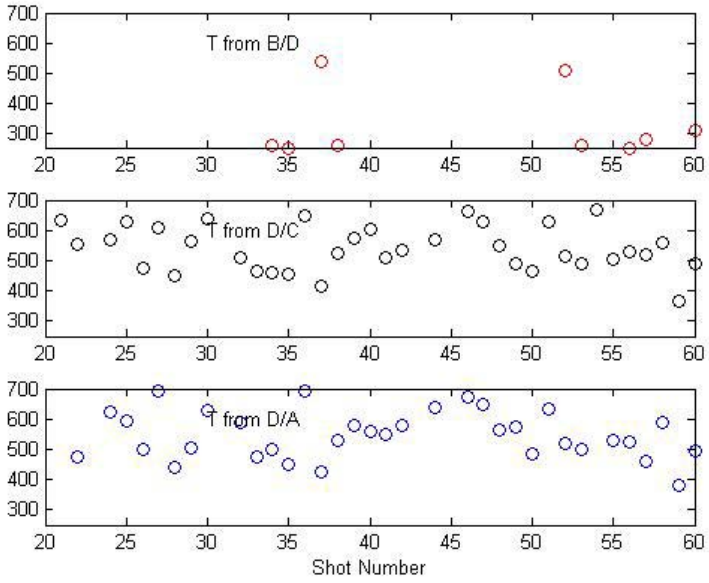

Figure 13. Single-shot TDLAS-based temperature measurements (T in K); same conditions as Figure 12

acquired.

The accuracy of TDLAS-derived quantities such as temperature can be ascertained via measurements made in steady-state environments with known controlled values or in similar environments in which the desired parameter is measured using a second known method. We have acquired water-based TDLAS measurements (using the transitions in Table 6) above a flat-flame burner along with corrected thermocouple measurements in the same methane/air flames at a fixed height above the burner surface. (This work will be discussed in detail in a future paper.) For the particular case of an equivalence ratio of 0.9, the TDLAS measurements yielded a path-integrated temperature across the burner of 1825 K using Boltzmann-plot data analysis. A sequence of thermocouple measurements made with three different bead diameters along the same path yielded a path-integrated temperature value of 1785 K. These two values agree with each other at the 2 % level. Similar accuracy assessments appear in the open literature. For example, in preparation for wind-tunnel testing of a model scramjet engine, researchers compared water-based TDLAS measurements of temperature with those of a thermocouple in a

premixed flame.[5] Over the temperature range of 1000 K to 1600 K they found the TDLAS-derived temperature to be a few percent greater than the thermocouple temperature with the difference increasing with flame temperature.

For measurements made in reacting flows – particularly those set up to test hardware – it is frequently not possible to obtain a secondary temperature measurement. Indeed, optical diagnostics are typically employed for temperature measurements in environments where other thermometry approaches are not possible or practical. It is prudent therefore to examine TDLAS data reduction strategies with regards to anticipated numerical scatter given finite signal-to-noise ratios in the context of apparent measurement scatter (i.e. precision). Such close examination can lead to conclusions that may be data-set dependent and care must be used in transferring such considerations between data sets.

Using transitions A, B and D of Table 6, the temperature of ambient laboratory air was measured following the Boltzmann plot and two-line approaches for extracting temperature. The data set included 1000 single scans of the employed diode lasers acquired at 1 kHz. The three derived average temperatures agreed to within 6%. (We note that the transitions of Table 6 are better suited for elevated temperature environments than for room temperature environments.) The Boltzmann plot average temperature of 293 K agrees with the two-line temperature (288 K) using the B/A line ratio at the 1.7% level. These three approaches yielded similar average values for the SNR-driven average uncertainty of ~33 K. However, the observed standard deviations of the derived temperatures were smaller, ~ 21 K. The larger SNR-driven uncertainty value is certainly due the relatively small signal associated with transitions B and D at room temperature.

Table 7. Extracted temperatures with associated uncertainties using Boltzmann analysis and area ratios for transitions of Table 1.

	Boltzmann Plot for A,B,C,D	Boltzmann Plot for A,B,C	B / C	B / A	B / D	A / C	D / C	D / A
avg. T (K)	488	425	427	437	300	371	479	503
std expt. (K)	72	49	35	38	104	122	58	68
avg. uncert. (K)	70	84	16	30	215	198	73	146

As an example of a measurement in a reacting flow, we examine a sequence of single-scan (single-shot) temperature acquired at the entrance to the isolator in a direct-connect hypersonic test facility. The measurements were made using a single line-of-sight across the mid-plane of the circular hardware just downstream of the Mach 1.8 facility nozzle. The incoming air stream consisted of heated (non-vitiated) air with an average water molecule number density of 6×10^{16} cm^{-3}. The data was collected at 1 kHz using the transitions noted in Table 6 and processed to yield values of the frequency-integrated absorbance for each shot. Temperatures were derived from these integrated areas using the area ratio approach (Eqn. 1 and 2) and the Boltzmann plot approach (Eqn. A 5). The four transitions provide for six unique area ratios. The derived temperatures for an arbitrarily chosen sequence of 40 shots are shown in Fig. 12 and 13 for the Boltzmann plot approach and five of the ratio-based approaches. As seen in Fig. 12, the results for the Boltzmann plot approach and the ratios of transition combinations B/A and B/C (see

Table 6 for transition labeling convention) follow each other quite closely. For example they each exhibit local maxima near shot numbers 23, 37, and 52 and local minima near 32 and 47. The apparent oscillation in temperature persists for all times recorded and probably reflects facility air supply characteristics such as compressor surge. Temperatures derived from area ratio combinations involving transition D (B/D, D/C, and D/A) exhibit large fluctuations (see Fig. 13) and don't reproduce the periodic structure evident in Fig. 12. Transition D exhibited the lowest signal-to-noise ratio observed for this data set and is the likely reason behind the excessive scatter seen in Fig. 13.

Using a full second worth of data (1000 shots), the average temperature was calculated for each approach along with the standard deviation of the measurements. These values are shown in Table 7. Similarly, the table includes the average of the uncertainties of the derived temperature values based on measured signal-to-noise ratios and the procedures detailed in the Appendix. Since the signal-to-noise ratio can include systematic error sources we do not add the individual uncertainties in quadrature but rather report the simple average. Note that the Boltzmann plot derived temperature using all four transitions exhibits larger observed scatter than that of the same plot with transition D eliminated. The temperature derived from the three-transition Boltzmann analysis is plotted in Fig. 12.

As anticipated from Figure 12 and Figure 13, the observed experimental scatter (standard deviation) as well as the anticipated numerical scatter are least for the three-transition Boltzmann approach and the ratio combinations of B/C and B/A. The mean temperatures derived via these three approaches agree within 2.8%. The aforementioned oscillation of the temperature accounts for the measured scatter being larger than the anticipated numerical scatter. The two area ratio approaches exhibit less measured scatter as well as less anticipated numerical uncertainty. Likewise, as anticipated from Fig. 13, temperatures derived from area ratios involving transition D exhibit widely varying mean values along with large measured scatter and large anticipated scatter.

The primary quantities derived from a TDLAS measurement are the temperature and number density of the target species. Numerous other quantities can be derived as well; for example, the pressure which is derivable from the line width of an absorption transition. The relevant expressions are shown in Appendix Eqn. A12 – A17 where use has been made of empirical relationships between the full width at half maximum of the transition, the temperature, and the pressure. The uncertainty in the derived pressure is then dependent upon the uncertainty in the derived temperature and measured line width. We take, as an example, the measured temperature of Table 7 (430 K) and the Voigt line width of the 7185.6 cm^{-1} transition (0.067 cm^{-1}) along with constant values of To=296 K, n = 0.65, and γo = 0.041 cm^{-1}/atm taken from the literature[21] to find a measured pressure of 0.9 atm. Assuming no uncertainty in the empirical constants, the uncertainty in the derived value of the pressure is 0.07 atm for a 10% temperature uncertainty and a 5% line width uncertainty. That is, the combined effects of temperature and line width uncertainty lead to an 8% pressure uncertainty.

For large data sets with thousands of single-shot spectra to be analyzed it is helpful to develop routines that afford some means of rejecting compromised spectra. Degradation can occur for multiple reasons such as gross beam steering or obscuration or transient electronic noise. One such approach that we have found valuable is close examination of the fitting associated with the Boltzmann plot. The scatter about the linear fit can be quantified using the standard rules for

calculating χ^2. For a single data set at constant flow condition we calculate the individual values of χ^2, average them, and then reject outliers that show large deviation from this average.

While issues associated with the accuracy, precision, and scatter associated with flow field parameters derived from TDLAS measurements have been discussed here using specific data sets, the methodology is quite general and can be extended to other data sets. We recommend using a combination of Boltzmann plot analysis combined with integrated area ratio analysis to extract the local path-integrated temperature. For a set of transitions it is best to exclude a transition or transitions that exhibit poor signal-to-noise ratios as compared to other transitions in the set. As indicated in Table 7, calculation of the anticipated numerical scatter provides guidance in selecting line pairs for careful analysis.

5.0 CONCLUSIONS AND RECOMMENDATIONS

The efforts described here lays detailed groundwork for the use of TDLAS in studying the dynamic behavior of scramjet isolators. An example of detailed measurements of shock train dynamics was presented. Such work provides invaluable information for anchoring CFD codes and related fluidic models. As yet, there is no comprehensive theory of all aspects of isolator performance and behavior preventing detailed prediction. For example, it is not now possible to accurately predict isolator margin given values for combustor heat release and pressure fields. TDLAS provides a tool to address the lack of fundamental information which will lead to desired comprehensive understanding.

Future work should strive to mature the TDLAS technique in three areas: 1) benchmarking of TDLAS derived physical parameters such as temperature with those obtained from other means, 2) broadening and refinement of the basic spectroscopic database for species such as water and molecular oxygen to improve the accuracy of available spectroscopic constants, and 3) development of advanced numerical algorithms for extracting spatiotemporal information from TDLAS measurements made along two or more lines of sight. Area 1 serves to facilitate the future use of TDLAS by researchers who do not traditionally use spectroscopic techniques. Benchmarking TDLAS measurements against other sensor/metrology standards gives such users a sense of expected performance. The aim of work in area 2 is to improve the accuracy of parameters derived from TDLAS measurements. The ultimate accuracy cannot be better than the spectroscopic parameters used in the TDLAS data processing routines. For example it is highly desirable to have tables of absorption cross sections with intrinsic accuracies better than 1%. Efforts in area 3 will expand the utility of the technique making comparison to modeling efforts much more sophisticated and hence valuable.

6.0 REFERENCES

1 Hanson, R. K., Jeffries, J. B., "Diode Laser Sensors for Combustion and Propulsion Flows, "JANNAF-41st CS/29th APS/23rd PSHS, San Diego, CA, (Dec. 2006).

2 Furlong, E. R., Mihalcea, R. M., Webber, M. E., Baer, D. S., Hanson, R. K., "Diode-Laser Sensors for Real-Time Control of Pulsed Combustion Systems," AIAA J. 37, pp 733-737 (1999).

3 Liu, J. T., Rieker, G. B., Jeffries, J. B., Gruber, M. R., Carter, C. D., Mathur, T., Hanson, R. K.,"Near-Infrared Diode Laser Absorption Diagnostic for Temperature and Water Vapor in a Scramjet Combustor," Appl. Opt.44, pp 6701-6711 (2005).

4 Williams, S., Barone, D., Barhorst, T., Jackson, K., Lin, K-C., Masterson, P., Zhao, Q., "Diode Laser Diagnostics for High Speed Flows," AIAA Paper 2006-7999, (2006).

5 Griffiths, A. D., Houwing, A. F. P., "Diode Laser Absorption Spectroscopy of Water Vapor in a Scramjet Combustor," Appl. Opt. 44, 6653-6659 (2005).

6 Lindstrom, C. D., Davis, D., Williams, S., Tam, C-J., "Shock-Train Structure Resolved with Absorption Spectroscopy Part 2: Analysis and CFD Comparison," AIAA J. 47, 2379-2390 (2009).

7 Bernath, P. F., Spectra of Atoms and Molecules, Second ed., New York, NY: Oxford University Press, 2005.

8 Herzberg, G., Molecular Spectra and Molecular Structure I. Spectra of Diatomic Molecules, Second ed., Malabar, FL.: Krieger Publishing Company, 1950.

9 Mukamel, S., Nonlinear Optical Spectroscopy, New York, NY: Oxford University Press, 1995.

10 Rothman, L. S., et al, "The HITRAN molecular spectroscopic database and HAWKS (HITRAN atmospheric workstation): 1996 edition," J. Quant. Spectrosc. Rad. Transfer 60, 665-710 (1998).

11 Rothman, L. S., et al, "The HITRAN 2004 Molecular Spectroscopic Database," J. Quant. Spectrosc. Rad. Transfer 96, 139-204 (2005).

12 Humlicek, J., "Optimized Computation of the Voigt and Complex Probability Functions," J. Quant. Spectrosc. Rad. Transfer 27, 437-444 (1982).

13 Liu, X., Jeffries, J. B., Hanson, R. K., "Measurement of Nonuniform Temperature Distributions Using Line-of-Sight Spectroscopy," AIAA J.45, 411-419 (2007).

14 Ouyang, X., Varghese, P. L., "Line-of-Sight Absorption Measurements of High Temperature Gases with Thermal and Concentration Boundary Layers," Appl. Opt. 28, 3979-3984(1989).

15 Wondraczek, L.,et al, "Mid-Infrared Laser-Tomographic Imaging of Carbon Monoxide in Laminar Flames by Difference Frequency Generation," Comb. Flame 138, 30-39 (2004).

16 Chung, K., Wolga, G. J., "Experimental Reconstruction of the Spatial Density Distribution of a Nonreacting Flow with a Small Number of Absorption Measurements," Appl. Opt. 34, 5492-5500 (1998).

17 Lindstrom, C. D., Tam, C-J., Davis, D., Williams, S., "Diode Laser Absorption Tomography of 2D Supersonic Flow," 43rd AIAA/ASME/SAE/ASEE Joint Propulsion Conference & Exhibit AIAA-2007-5014, (2007).

18 Torniainen, E. D. , Gouldin, F. C., "Tomographic Reconstruction of 2-D Absorption Coefficient Distributions from a Limited Set of Infrared Absorption Data," Combust. Sci. and Tech. 131, 85-105(1998).

19 Torniainen, E. D ., Hinz, A. K. , Gouldin, F. C ., "Tomographic Analysis of Unsteady, Reacting Flows: Numerical Investigation," AIAA J. 36, 1270-1278 (1998).

20 Durry, G., et al , "Pressure-Broadening Coefficients and Line Strengths of H2O Near 1.39 um: Application to the In Situ Sensing of the Middle Atmosphere with Balloonborne Diode Lasers," J. Quant. Spectrosc. Rad. Transfer 94, 387-403 (2005).

21 Liu, X., Zhou, X., Jeffries, J. B., Hanson, R. K., "Experimental Study of H2O Spectroscopic Parameters in the Near-IR (6940-7440 cm-1) for Gas Sensing Applications at Elevated Temperature," J. Quant. Spectrosc. Rad. Transfer 103, 565-577 (2007).

22 Lepere, M., Henry, A., Valentin, A., Camy-Peyret, C., "Diode-Laser Spectroscopy: Line Profiles of H2O in the Region of 1.39 um," J. Mol. Spectrosc. 208, 25-31 (2001).

23 Toth, R. A., "Extensive Measurements of H2O Line Frequencies and Strengths: 5750 to 7965 cm-1," Appl. Opt., 4851-4867 (1994).

24 Delaye, C., Hartmann, J-M., Traine, J., "Calculated tabulations of H2O line broadening by H2O, N2, O2, and CO2 at High Temperature," Appl. Opt. 28, 5080-5087 (1989).

25 Nagali, V., Chou, S. I ., Baer, D. S ., Hanson, R. K ., "Diode-Laser Measurements of Temperature-Dependent Half-Widths of H2O Transistions in the 1.4 um Region," J. Quant. Spectrosc. Radiative Transfer 57, 795-809 (1997).

26 Gamache, R. R., Hartmann, J-M., Rosenmann, L., "Collisional Broadening of Water Vapor Lines - I. A Survey of Experimental Results," J. Quant. Spectrosc. Rad. Transfer 52, 481-499 (1994).

27 Gruber, M., et al, "Newly Developed Direct-Connect High-Enthalpy Supersonic Combustion Research Facility," J. Propul. Power 17, 1296-1304 (2001).

28 Mathur, T., et al, "Supersonic Combustion Experiments with a Cavity-Based Fuel Injector," J. Propul. Power 17, 1305-1312 (2001).

APPENDIX

The following indicates the manner in which the numerical uncertainties in the derived values of temperature, target species number density and pressure discussed above are found using standard statistical analysis for both the line ratio approach and the Boltzmann plot approach.

The uncertainties in the measured absorption signals (A) denoted by σA are determined from signal-to-noise conditions as noted above. For any function f that is dependent upon A or a set of A_is, the uncertainty in f is determined from the following

$$\sigma f^2 = \sum_{i=1}^{n} \sigma z_i^2 \left(\frac{\partial f}{\partial z_i}\right)^2 \quad \text{A1)}$$

where z_i denotes A_i or a function of A_i. Note, we are presuming independence of the variables z_i. Herein, the uncertainty (σ) is expressed as a standard deviation. The 95% confidence interval can be found from σ through multiplication by 1.96.

We first consider the uncertainty in the temperature derived from a two-line ratio. Defining the ratio of the integrated absorbances as $R = A_1/A_2$, the fractional temperature uncertainty can be written from Eqn. 1 and Eqn. 2 as

$$\frac{\sigma T}{T} = \frac{{}^{k}/_{\Delta E}}{{}^{k}/_{\Delta E} \; ln\left(R \; {}^{LS_2(To)}/_{LS_1(To)} \right) + {}^{1}/_{To}} \sigma R \quad \text{A2)}$$

where $\Delta E = E_1 - E_2$. Similarly, the uncertainty in the extracted number density can be expressed via

$$\sigma N^2 = \left[\left(\frac{1}{LS\, L}\right)^2 \sigma A^2 + \left(\frac{\partial N}{\partial\, LS} \frac{\partial\, LS}{\partial T}\right)^2 \sigma T^2 \right]^2 \quad \text{A3)}$$

$$\frac{\partial N}{\partial\, LS} = \frac{-A}{LS^2\, L} \qquad \frac{\partial\, LS}{\partial T} = LS(To) \; \frac{Q(To)}{Q(T)} \; e^{-\frac{E}{k}\left(\frac{1}{T}-\frac{1}{To}\right)} \quad \text{A4)}$$

A Boltzmann analysis of absorption spectra stems from the following expression for each (i^{th}) transition in the spectrum (we omit factors associated with stimulated emission that are insignificant in this context)

$$ln\left[\frac{A_i}{S_i\,(T_o)}e^{-\frac{E_i}{k\,T_o}}\right] \;=\; -\frac{E_i}{k\,T} \;+\; ln\left[\frac{Q(T_o)}{Q(T)}\;N\;L\right] \qquad \text{A5)}$$

where *To* denotes a reference temperature (usually 296 K). A Boltzmann plot is generated by graphing the left hand side of Eqn. A5 as a function of E_i for two or more transitions. A linear fit to the plotted points yields the temperature (T) via the slope and the number density (N) of the target species via the y intercept. To extract a measure of the uncertainty in the derived values for T and N, we write the linear fit to the Boltzmann plot in the form $y = a + b\,x$. Uncertainties in a and b are derivable from the uncertainties in the values of y that in turn reflect the uncertainties in the set of A_i. A solution for a and b is found using well-established routines that we reproduce here following the notation of Press *et al.*[1] Each value of y_i has an associated uncertainty noted as σ_i.

$$S \;=\; \sum_{i=1}^{N}\frac{1}{\sigma_i^2} \qquad Sx \;=\; \sum_{i=1}^{N}\frac{x_i}{\sigma_i^2} \qquad Sy \;=\; \sum_{i=1}^{N}\frac{y_i}{\sigma_i^2} \qquad Sxx \;=\; \sum_{i=1}^{N}\frac{x_i^2}{\sigma_i^2} \qquad \text{A6)}$$

$$Sxy \;=\; \sum_{i=1}^{N}\frac{x_i y_i}{\sigma_i^2} \qquad \Delta = \; S\,Sxx \;-\; (Sx)^2 \qquad \text{A7)}$$

The fitted values of a and b along with their uncertainties are then given by

$$a \;=\; \frac{Sxx\;Sy \;-\; Sx\;Sxy}{\Delta} \qquad b \;=\; \frac{S\;Sxy \;-\; Sx\;Sy}{\Delta} \qquad \text{A8)}$$

$$\sigma a^2 \;=\; \frac{Sxx}{\Delta} \qquad \sigma b^2 \;=\; \frac{S}{\Delta} \qquad \text{A9)}$$

Following a Boltzmann analysis, the uncertainty in the derived value for the temperature and target species number density are given from the above by

$$\sigma T \;=\; \frac{\sigma b}{k\,b^2} \;=\; \frac{1}{k}\;\frac{\sqrt{S}\;\Delta^{1.5}}{(S\;Sxy \;-\; Sx\;Sy)^2} \qquad \text{A10)}$$

[1] Press, W. H., Teukolsky, S. A., Vetterling, W. T., Flannery, B. P., Numerical Recipes in C++, Chap. 15, (Cambridge University Press, Cambridge, England, 2002).

$$\sigma N \quad = \quad \frac{Q(T)}{Q(To)} \; \frac{e^{a}}{L} \; \sigma a \qquad \text{A11)}$$

TDLAS measurements can be used to determine the local pressure through the line widths (full width at half maximum) of the recorded spectral transitions. Under the physical environments associated with hydrocarbon-based reacting flows, the spectral line shapes are well characterized by the Voigt spectral profile. This profile includes line broadening due to temperature (Doppler broadening) as well as pressure (collision broadening). The collision broadening contribution to the line width can be separated from the total line width and Doppler contribution as follows

$$\Delta\nu_L \quad = \quad \frac{\Delta\upsilon_V^2 \; - \; \beta^2 \, T}{\Delta\nu_V} \qquad \text{A12)}$$

where β denotes constants associated with Doppler width expression ($\Delta\nu_D = \beta \, T^{1/2}$). Careful experimental work has revealed scaling laws that empirically show the relationship between the collision width and the pressure that are often written in the following form

$$P \quad = \quad \frac{\Delta\nu_L}{2\,\gamma} \qquad \gamma \; = \; \gamma_o \; \left(\frac{T_o}{T}\right)^{n} \qquad \text{A13)}$$

where n and γ_o are transition-specific constants and T_o the reference temperature. The above can be combined into a single expression

$$P \quad = \quad \frac{1}{2\,\gamma_o \, T_o^n} \; \left[T^n \; \left(\Delta\nu_V - \frac{\beta^2}{\Delta\nu_V} \, T\right)\right] \qquad \text{A14)}$$

The statistical uncertainty in the pressure can then be found from

$$\sigma P^2 \quad = \quad \left(\frac{\partial P}{\partial T}\right)^2 \; \sigma T^2 \; + \; \left(\frac{\partial P}{\partial \, \Delta\nu_V}\right)^2 \; \sigma \Delta\nu_V^2 \qquad \text{A15)}$$

$$\frac{\partial P}{\partial \Delta\nu_V} \quad = \quad \frac{1}{2\,\gamma_o \, T_o^n} \; \left[T^n \; + \; \frac{\beta^2 \, T^{n+1}}{\Delta\nu_V{}^2}\right] \qquad \text{A16)}$$

$$\frac{\partial P}{\partial T} \quad = \quad \frac{1}{2\,\gamma_o \, T_o^n} \; \left[T^{n-1} \; \Delta\nu_V \; n \; - \; \frac{\beta^2 \, T^n \, (n+1)}{\Delta\nu_V}\right] \qquad \text{A17)}$$